



Impacts of urban expansion on fog types in Shanghai, China: Numerical experiments by WRF model



Ying Gu^a, Hiroyuki Kusaka^{b,*}, Van Quang Doan^c, Jianguo Tan^d

^a School of Air Transportation, Shanghai University of Engineering Science, Shanghai 201620, China

^b Center for Computational Sciences, University of Tsukuba, 1-1-1 Tennodai, Tsukuba, Ibaraki 305-8577, Japan

^c Center for Climate Research Singapore, 537054, Singapore

^d Shanghai Meteorological Service, Shanghai Climate Center, Shanghai 200030, China

ARTICLE INFO

Keywords:

Urban expansion

WRF

Climatological characteristics

Fog event

Fog type

Shanghai

ABSTRACT

Fog is a hazard to transportation activities in Shanghai, China, but it is not known how this fog is influenced by urban expansion. Here we use a numerical model to run, for the first time for Shanghai, sensitivity experiments of the fog response to urban expansion, including the changes of land use and anthropogenic heat. Instead of using 'fog days' as a measure, we use the 29-year (1989–2017) meteorological observations of fog events at Hongqiao International Airport in central Shanghai, and classify the fog into radiation, advection, advection–radiation, and precipitation types. The results show that (1) Fog events generally decrease over these 29 years, with the decline in winter accounting for 50.2% of the total reduction. (2) Radiation fog decreases the most, but remains the most common type throughout the period. (3) Numerical sensitivity experiments show that the urban expansion in the past 29 years caused both an increase in surface air temperature and a decrease in water-vapor mixing ratio, resulting in a decrease in relative humidity and an increase in visibility for radiation fog. (4) For advection fog, the increased surface air temperature allowed an increase in water-vapor mixing ratio, but a decrease in liquid water. (5) Due to warmer near-surface air, the inversion layer weakened. Hence, urban expansion in Shanghai has reduced the amount of not only radiation fog, but also advection fog.

1. Introduction

Fog is a well-known hazard to transportation activities such as airline and automobile travel. Shanghai, on the eastern coastline of China, is particularly influenced by fog events at its two international airports and on its highways, especially from late autumn to early spring. The resulting flight delays and cancellations are costly to the airlines, and the travel disruptions increase the congesting and disorder at the airports. On the highways, the dense fog can lead to fatal accidents; for example, the accidents during the dense fog of 6 November 2016 that killed 9 people and injured over 40 others. Thus, fog clearly influences these urban activities, but how does urban expansion influence the occurrence of fog?

Climatological studies of fog based on long-term observations and statistical analyses help reveal fog characteristics, trends, and related correlations. For instance, Vautard et al. (2009) and Van Oldenborgh et al. (2010) examined the horizontal visibility from over 300 stations in Europe, finding that fog, mist, and haze declined in the past 30 years, a trend that correlated with trends in sulfur dioxide emissions.

Similarly, Witiw and LaDochy (2008) and LaDochy and Witiw (2012) revealed a decrease of dense fog in the greater Los Angeles area for the period 1948–2004, but here the decline was correlated to the Pacific Decadal Oscillation index and the El-Niño Southern Oscillation. For the North China Plain, Fu et al. (2014) examined 30 years of data of low visibility, fog, and haze, finding a positive fog trend before 1995, a stable level from 1995 to 2003, and a strong negative trend after 2003. The variation was associated with wind and relative humidity (RH). For South Korea, Belorid et al. (2015) investigated the fog trend, finding a significant decrease in 10 stations due to the reduction of radiation fogs. Similar research has been done in other regions, including Greece (Stolaki et al., 2009), Japan (Akimoto and Kusaka, 2015), and France (Dupont et al., 2016). Although these climatological studies have all found a decreasing trend of fog, some have instead found an increasing trend in fog frequency. For example, two stations in the south-eastern United States (Forthun et al., 2006) and one station at the summit of Mount Washington in the north-eastern United States (Seidel et al., 2007) experienced an increase in annual fog. Also, the frequencies of winter fog events have doubled over eastern-central China during the

* Corresponding author.

E-mail address: kusaka@ccs.tsukuba.ac.jp (H. Kusaka).

past 30 years, an increase due to both the weakened East Asian winter monsoon circulation and the increased regional atmospheric aerosol loading (Niu et al., 2010). A positive fog trend was also detected in south Asia in winter from 1976 to 2010 (Syed et al., 2012).

Studies indicate that three main factors influence fog trends: global climate change (Chen et al., 2006; Witw and LaDochy, 2008; Niu et al., 2010; LaDochy and Witw, 2012; Syed et al., 2012; Baldocchi and Waller, 2014), urban heat island (UHI) (Li et al., 2012; Belorid et al., 2015; Williams et al., 2015), and air pollution (Shi et al., 2008; Vautard et al., 2009; Van Oldenborgh et al., 2010; Niu et al., 2010; Baldocchi and Waller, 2014; Klemm and Lin, 2016). The last two factors relate to urban expansion. In particular, urban expansion modifies the local climate with increasing temperature and decreasing moisture due to land-use changes and the release of anthropogenic heat (AH), resulting in less fog formation. On the other hand, urbanization can increase air pollution, resulting in an increase in fog days.

Shanghai has experienced particularly rapid urbanization since 1978. From 1978 to 2015, the population doubled, and from 1980 to 2015, the electricity consumption increased nine-fold. Along with this urbanization, researchers found a long-term decreasing trend of fog days, and associated this trend with the UHI (Zhou and Zheng, 1987; Jin and Shi, 2008). However, these studies did not determine the exact mechanism through which the UHI influenced this trend.

Our first objective here is to determine how the changes of land use and AH affect fog events in Shanghai for the first time. As part of this objective, we classify the fog events into specific types and examine the long-term trends of each type. We begin, in section 2, by describing the method, including the data and the numerical model. Section 3 has the climatology of fog in Shanghai based on the 29-year records at Hongqiao International Airport (SHA). Section 4 has the settings of the weather research and forecasting (WRF) model and experimental design. Section 5 shows the results from the numerical simulation of a radiation fog event by WRF. Section 6 is similar to section 5, but for advection fog. In the last sections, we discuss the implications and give conclusions.

2. Data and method

2.1. Data

2.1.1. Hourly meteorological observations

We use two datasets. One is the hourly/sub-hourly observation dataset of climate data online (CDO) from the National Oceanic and Atmospheric Administration (NOAA) National Centers for Environmental Information (NCEI). This data includes visibility, surface air temperature, dewpoint temperature, wind velocity, ceiling height, cloud cover, and weather codes, all of which are derived from meteorological terminal aviation routine weather reports (METARs) at airports. This hourly dataset contains 239,848 records, 91.3% of which have visibility data. All data pass quality control checks. Specifically, data from Hongqiao International Airport in central Shanghai for 1989–2017 are used to identify and classify the fog events. In addition, data of the calculated relative humidity are also available in this dataset. We use to evaluate the model performance together with data of surface air temperature, wind, and visibility.

The other dataset is hourly observations in Shanghai operated by the Shanghai Meteorological Bureau (SMB). They include the observed records of the above variables except weather codes. All data are complete and subject to SMB stringent quality controls.

Data at three stations are used here to further evaluate the numerical simulation: Xu Jia Hui station, an urban site (XJH); the Hongqiao International Airport, a rural–urban site (SHA); and Chong Ming station, a rural site (CM) (Fig. 1a, b). Data from the other sites are used to show spatial distributions of observed and simulated surface air temperature, relative humidity, and visibility.

2.1.2. Shanghai land use and land cover (LULC)

For data on Shanghai's land use and land cover, hereafter LULC, we use the MEGA-WEB GIS platform (Gong et al., 2017) with a resolution of 30 m for the years of 1988 (Fig. 1a) and 2013 (Fig. 1b). Urban fractions are calculated from LULC data as shown in Fig. 1c (for 1988) and Fig. 1d (for 2013). Here, urban fraction, taken as the index of urban expansion, equals the areal fraction that is urban in a model grid cell. The two figures show a rapid urban expansion from the city centre to rural areas.

2.1.3. Anthropogenic heat (AH)

We use data from statistical yearbooks to estimate AH values for the model. First, the annual AH is calculated using Eq. 1. The per capita AH is then calculated from AH as Eq. (2). Then, following the treatment of the urban canopy model (UCM) in Kusaka et al. (2001), we classify the area into commercial area, high-density residential area, and low-density residential area. The districts in Shanghai are assigned to three urban categories according to population density for each district. The total area (population) for each urban category can be added using the data of area (population) for each district. Thus, we can estimate the population density for each urban category using Eq. 3. Finally, we use Eq. 4 to calculate AH for each urban category. Considering sensitivity experiments in the following discussion, we also estimate AH for LULC in 2013 using annual AH for 1988. The resulting values for 1988 and 2013 are in Table 1.

$$\text{Annual AH} = \text{total energy consumption} \times \text{energy conversion efficiency} \times \text{heat rate of coal} \quad (1)$$

$$\text{per capita AH} = \text{annual AH}/\text{total population} \quad (2)$$

$$\begin{aligned} &\text{Population density (each urban category)} \\ &= \text{population (each urban category)}/\text{area (each urban category)} \end{aligned} \quad (3)$$

$$\begin{aligned} \text{AH (each urban category)} &= \text{per capita AH} \\ &\times \text{population density (each urban category)} \end{aligned} \quad (4)$$

2.2. Fog identification

2.2.1. Identification of fog occurrence, dense fog, and fog events

This study adopts the definition of fog events developed by Tardif and Rasmussen (2007). In particular, 1.6 km is used as the threshold visibility for fog occurrence, and 1.0 km for dense fog. Thus, fog occurrence includes mist and ice fog. A fog event requires that five consecutive hourly observations include at least three with fog occurrence with at least one of those being dense fog. To distinguish the fog and haze, we will use both visibility and weather codes to classify the fog types.

2.2.2. Classification of fog

We classify the fog into four types: radiation, advection, advection–radiation, and precipitation (Zhou et al., 1981). Our algorithm is modified from those of Tardif and Rasmussen (2007) and Akimoto and Kusaka (2015). In particular, the category of precipitation fog here is a generalization of frontal fog types (Zhou et al., 1981). Table 2 lists the main criteria used for the classification and the associated primary mechanisms for fog formation of each type. For example, an advection–radiation fog forms when an air mass moves from sea to inland and is cooled radiatively during the night (Byers, 1959). This fog type differs from a radiation fog because the increase of water vapor during an advection–radiation fog increases the water-vapor pressure and dewpoint temperature (Zhou et al., 1981). Taking Table 2 as a reference, we use a decision tree in the fog-type classification (Fig. 2). As the data of cloud ceiling and cloud cover are missing, it is difficult for us

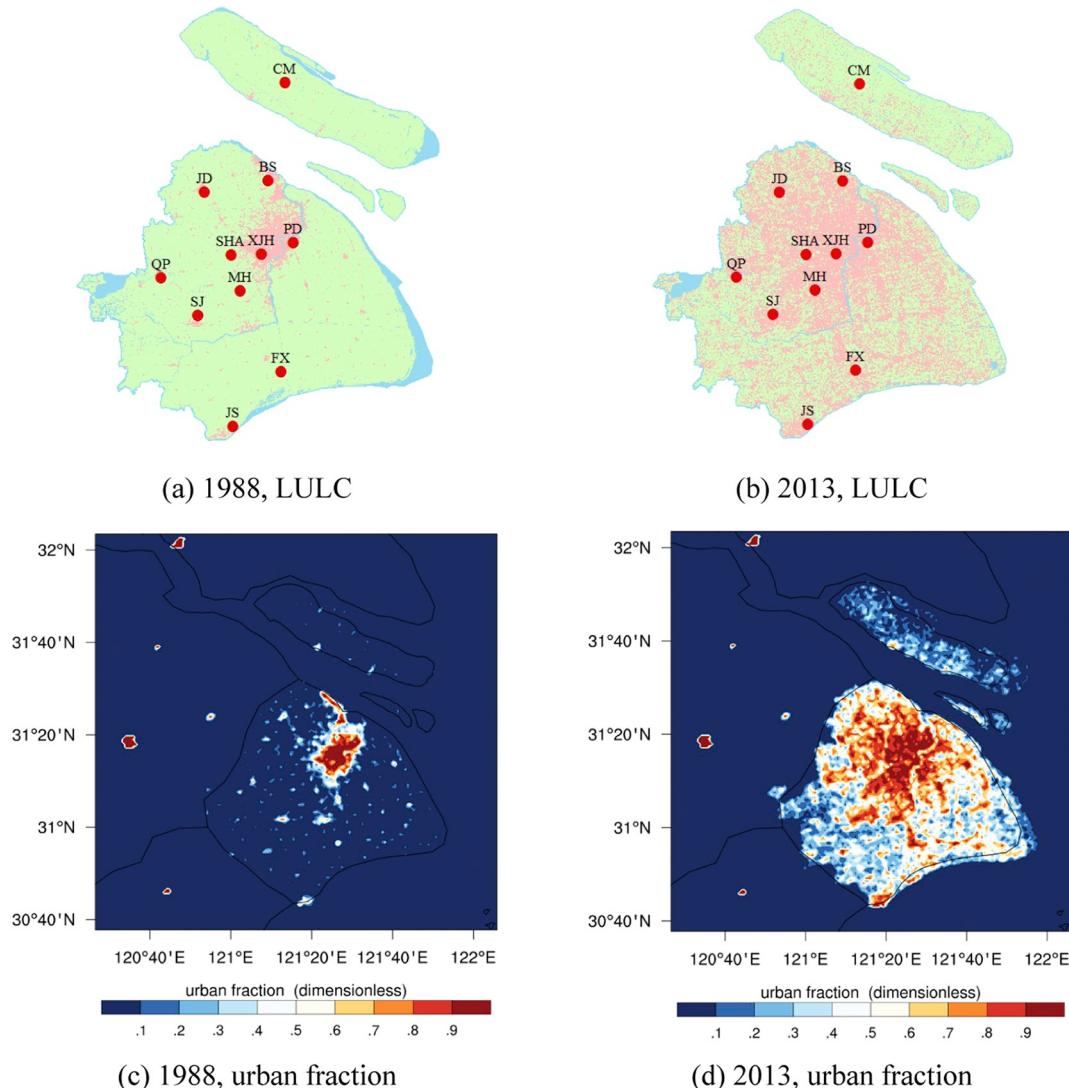


Fig. 1. Distribution of LULC and urban fraction in Shanghai. (a) LULC in 1988. (b) LULC in 2013. (c) Urban fraction in 1988. (d) Urban fraction in 2013. In (a) and (b), pink is urban, green is non-urban, and blue is water. The red points are observation stations. The airport is marked SHA. (For interpretation of the references to colour in this figure legend, the reader is referred to the web version of this article.)

to consider the condition of clear sky in the current algorithm. Thus, Fig. 2 is not completely consistent with Table 2.

3. Climatological characteristics of fog at SHA

3.1. Annual variation of fog types

From 1989 through 2017, we identified 467 fog events, with 89.3% of them classified by type. We will refer to 1989–1998 as the past period and 2008–2017 as the present from the point view of time. We noticed a big step from 2008 to 2009, and confirmed that the

measurement method did not change between those two years. The big drop might be related to the large scale effect.

For the present period, radiation fog is the most common type, accounting for 38.3% of all fog events (Fig. 3). Advection fog and advection–radiation fog follow radiation fog with percentages 27.7% and 23.4%, respectively. Precipitation fog is the least common type, corresponding to 8.5% of all fog events.

Among all four types of fog, radiation fog events dominate most years. However, as shown in Fig. 4, they decrease significantly during the past 29 years with a significance level of 0.001 for *t*-test. During 1989–1998, we identified 95 radiation fog events, but during

Table 1
Estimated anthropogenic heat for 1988 and 2013.

Scenario	Anthropogenic heat ($\text{W}\cdot\text{m}^{-2}$)		
	Commercial	High density residential	Low density residential
AH 1988 for LULC 1988	48	9	1
AH 1988 for LULC 2013	23	7	2
AH 2013 for LULC 2013	96	31	7

Table 2

Main criteria for the classification of fog events and associated primary mechanisms for fog formation of each type.

Fog type	Criteria	Primary mechanism	Reference
Precipitation (PCP)	Precipitation recorded at fog onset or the hour prior	Thermodynamic influence of evaporating precipitation	Tardif and Rasmussen, 2007; Belorid et al., 2015
Radiation (RAD)	① Wind speed < 6 mph (2.682 m/s) ② Clear sky (not considered in current work) ③ Cooling before onset, or slight warming in the hour leading to fog onset if preceded by cooling ④ Onset between the hour prior to sunset and before sunrise	Radiative cooling over land	Tardif and Rasmussen, 2007; Akimoto and Kusaka, 2015; Belorid et al., 2015
Advection (ADV)	① Wind speed ≥ 6 mph (2.682 m/s) ② Sudden decrease in visibility ③ Onset like a wall approaching the station	Mixing caused by the advection of different air masses of contrasting temperatures as moist, warm air comes in contact with a colder water or land surface	Tardif and Rasmussen, 2007; Akimoto and Kusaka, 2015;
Advection-radiation (ADV-RAD)	① Wind speed < 6 mph (2.682 m/s) ② Clear sky (not considered in current work) ③ Cooling before onset, or slight warming in the hour leading to onset if preceded by cooling ④ Onset between sunset and sunrise ⑤ Water vapor pressure increase before fog onset	① Radiative cooling over land during night ② Similar to advection fog	Zhou et al., 1981; Belorid et al., 2015

2008–2017, we identified only 18. Advection fog events are presently the second most common type, but were less common than advection–radiation fogs before 2008 (Fig. 3). Although the trend in advection fog events is not clear, this fog type decreases by 50% from the past to the present periods. In contrast, the advection–radiation fog decreases significantly after 2008. In particular, the past period had 52 advection–radiation fog events, whereas the present period has just 11. For precipitation fog, the number of events is small before 1994, then increases and maintains a high level until 2001, and then decreases, having only 4 events in 2008–2017. Compared to the past period, this is a decrease in precipitation fog by 91.7%.

Due to the decrease in each type of fog, the total number of fog events has also decreased. The annual mean number of fog events is 16.1 over all 29 years. The number exceeds 30 events in 1994 and 1997, but no fog events occur in 2012 and 2017. The past period (1989–1998) has an annual mean of 24.8, whereas the present period (2008–2017)

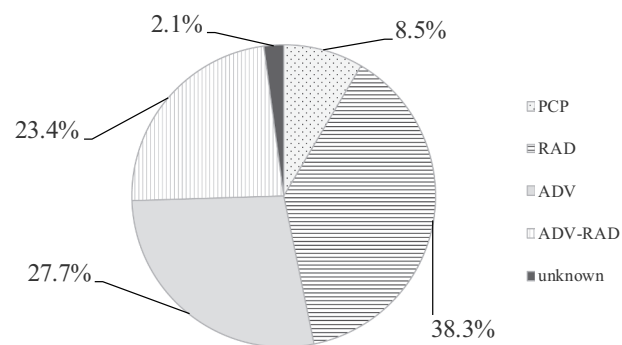


Fig. 3. Percentages of fog types in the present period (2008–2017).

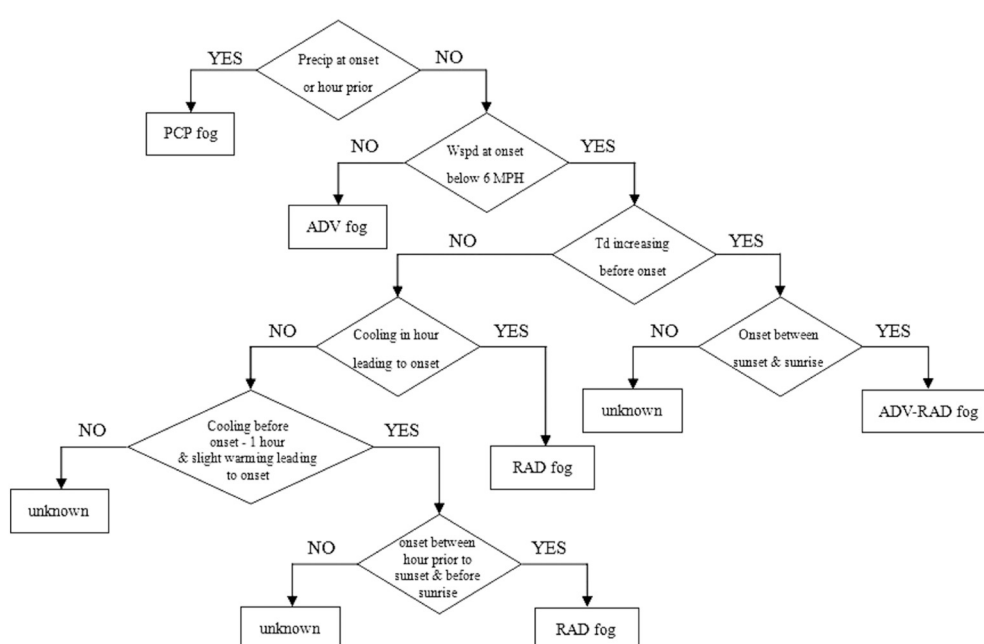


Fig. 2. Algorithm for classifying fog types.

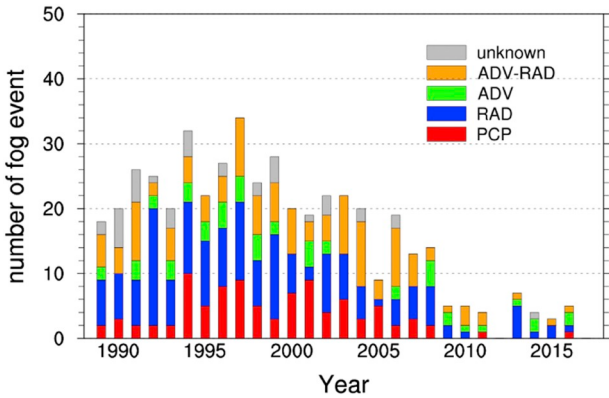


Fig. 4. Annual number of the four types of fog events.

has only 4.7. This decrease in total fog has a significance level of 0.01 for the Pearson's correlation coefficient.

3.2. Seasonal variation of fog types

Consider now the seasonal variation of the four fog types. All fog types occur least in August, both in the past and present periods (Fig. 5). Radiation fog events occur throughout the whole year except August, but are more frequent in winter and spring, particularly in the past period. Advection–radiation fog has a trend similar to that of radiation fog. In contrast, for advection fog, the number of events hardly vary by month. Except for the months of July to September, < 5 advection fog events occur every month. Finally, in the past period, precipitation fog events occur every month except August–October.

Consider now the season-by-season decline in fog events between the past and present periods. In winter (Dec–Feb), radiation fog decreases by 40 events, the most of all fog types. Second-most is precipitation fog by 18 events, followed by advection–radiation fog at 16, and advection fog at 3 events. Thus, the decline of fog in winter is mainly due to the reduction of radiation fog. In spring (Mar–May), the largest decrease comes from precipitation-fog events with a decline of 18, due to it disappearing in February through July in the present period. Following this decrease are radiation fog, by 14 events, advection–radiation fog by 7, and advection fog, also by 7 events. In autumn (Sep–Nov), radiation fog decreases by 18 events, advection–radiation fog by 13 events, precipitation fog by 5, and advection fog by only 2 events. Fog events declined the least in summer, compared with those in the other seasons.

Overall, almost every month saw a sharp reduction of fog events (Fig. 5). In the past period, fog events occurred throughout the whole year except August. However, in the present period, 95.7% of fog events

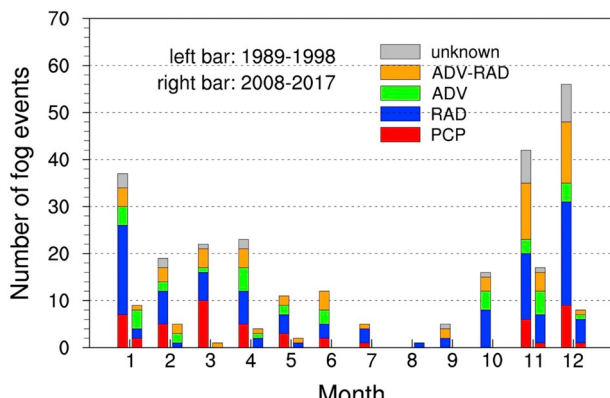


Fig. 5. Number of each type of fog event per month in the past (1989–1998) and present (2008–2017) periods.

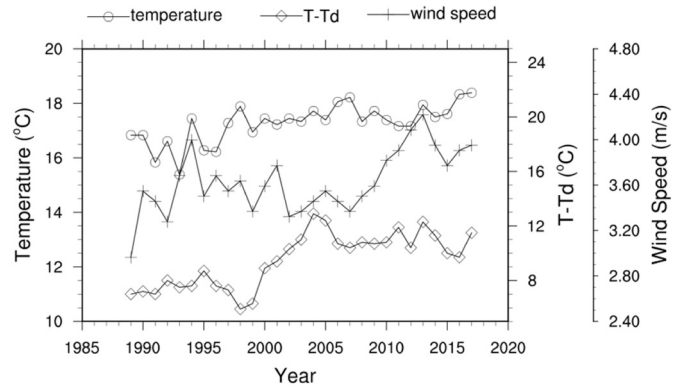


Fig. 6. Annual mean temperature, wind speed, and temperature minus dew-point at the rural–urban site SHA.

occur from November through May, with the top months being December, November, and January, in decreasing order. Overall, winter accounts for 50.2% of the reduction, followed by Spring at 26.9%. In the present period, fog events hardly occur from June to October.

3.3. Variation of meteorological variables

The formation and dissipation of fog is sensitive to meteorological variables, including temperature, humidity, and wind speed. During the past 29 years, the annual mean temperature and wind speed at the rural–urban station SHA have significantly increased (Fig. 6). In particular, compared to the past, the current annual mean temperature is 1.8 °C higher and the annual mean wind speed is higher by 0.3 m/s. In contrast, the mean annual dewpoint decreased by 1.8 °C, and thus, the difference between temperature and dewpoint increased by 3.6 °C, indicating a drying trend over the past 29 years. An increasing temperature, increasing wind speed, and decreasing humidity are all unfavourable for the formation of fog.

4. Model description and experimental design

4.1. Model configurations

We use the modified WRF-ARW model (version 3.1.1), coupled with a single-layer UCM, to examine how changes in land use and AH would have affected fog events. The modification of the WRF was done by Doan and Kusaka (2016). Unlike the standard version, the modified WRF can read 2-dimensional (2D) urban-fraction maps. The model was run with four nested domains with horizontal grid spacings of 27 km (164×164), 9 km (160×160), 3 km (160×160) and 1 km (160×160) (Fig. 7). The vertical grid contained 36 sigma levels from the surface to 100 hPa. Nine levels were set under 200 m.

The model includes several microphysics schemes, cumulus parameterizations, planetary boundary layer schemes, longwave radiation schemes, and shortwave radiation schemes that can significantly affect the simulated formation and dissipation of fog (Zhang et al., 2014a; Chaouch et al., 2017; Lin et al., 2017). To reduce uncertainty of the experiments, an ensemble method was used as shown in Table 3. The model was initialized with final (FNL) analysis data from the National Centers for Environmental Prediction (NCEP) with a horizontal grid spacing of 1° or from analysis data from the Japan Meteorological Agency's global spectral model (JMA-GSM) with a horizontal grid spacing of 0.5°. The main model configurations are shown in Table 3.

We selected schemes with big differences in the model's concept between the two. The different types of schemes should be chosen to understand robustness of the simulations, as well as uncertainty due to the selection of the model configuration. For microphysics, Kessler is the simplest warm rain scheme, while WSM6 is a complicated cold rain

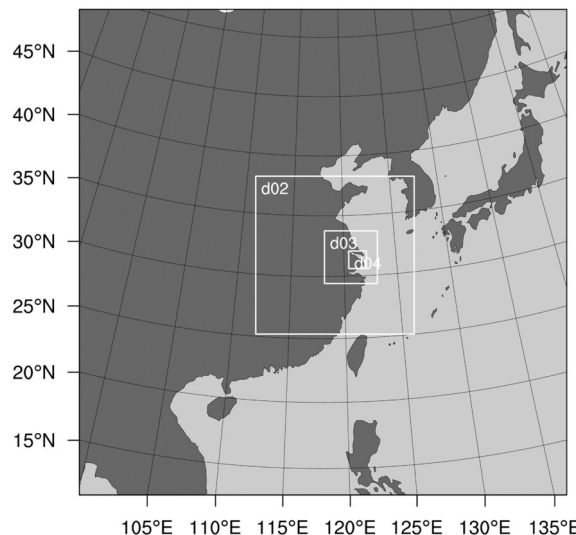


Fig. 7. Domain settings in the WRF model. The overall square is domain d01.

Table 3
Experimental schemes for the ensemble method.

Experiment	Land use	IC/BC/ LC	Microphysics	PBL	Longwave Radiation
1	2013	FNL	Kessler	MYNN L2.5	RRTM
2			WSM6	MYNN L2.5	RRTM
3			Kessler	YSU	RRTM
4			Kessler	MYNN L2.5	RRTMG
5		JMA-	Kessler	MYNN L2.5	RRTM
6		GSM	WSM6	MYNN L2.5	RRTM
7		ANAL	Kessler	YSU	RRTM
8			Kessler	MYNN L2.5	RRTMG
9	1988	FNL	Kessler	MYNN L2.5	RRTM
10			WSM6	MYNN L2.5	RRTM
11			Kessler	YSU	RRTM
12			Kessler	MYNN L2.5	RRTMG
13		JMA-	Kessler	MYNN L2.5	RRTM
14		GSM	WSM6	MYNN L2.5	RRTM
15		ANAL	Kessler	YSU	RRTM
16			Kessler	MYNN L2.5	RRTMG

scheme. For PBL, MYNN L2.5 is a local closure scheme, whereas YSU is a non-local closure scheme. For longwave radiation, RRTM does not consider aerosol condensational effect on clouds, which is integrated into RRTMG scheme. All schemes are widely used in fog simulations.

4.2. Experiment design

To investigate the responses of fog formation to urban expansion, we ran sensitivity experiments based on two sets of land-use parameters representing 2013 and 1988 (Table 4 and Table 5). Case URB2013 (experiments 1–8), taken as the control experiments, represents the current stage of urbanization using land use and AH data in 2013. Case URB1988 (experiments 9–16) are the experiments for the past urban scenario that use parameters of land use and AH for 1988. To eliminate the influences caused by different meteorological conditions (initial and

Table 5
Description of sensitivity experiments.

Case comparison	Description
LU2013 - URB1988	Impact of land-use change only
URB2013 - LU2013	Impact of AH change only
URB2013 – URB1988	Total impact of land-use and AH change

Table 6
Urban fractions calculated by WRF from the land use data for three types of land-use change and representative stations.

Type	Representative station	URB1988	URB2013
I	XJH	0.86	0.80
II	SHA	0.05	0.70
III	CM	0.09	0.15

boundary conditions of the atmosphere) and highlight the impacts of urban expansion, we used the meteorological conditions of 2013 for both cases. Both sets of experiments are also run with the same model configuration. Then, to help understand how the fog was influenced by the urban changes, we examine changes of fog from the differences between cases URB2013 and URB1988.

In addition, case LU2013 is designed to examine individual contributions of land-use and AH-emission change to surface air temperature. Experiments for case LU2013 are similar to those for case URB2013 except AH. The differences between cases are described in Table 5.

The urban fractions for the three sites have changed differently. As shown in Table 6, XJH has been an urban site at least since 1988, but was less urbanized in 2013. In contrast, SHA was rural around 1988, but has since experienced rapid urbanization. CM is located further away from the city centre. Its level of urbanization is relatively low. Then, three types of land-use change and representative stations are described in Table 6.

5. Radiation fog case

In the present ten-year period, radiation fog accounts for over 38.3% of fog events in Shanghai (Fig. 3) and has decreased the most during the past 29 years. The main physical mechanism for the formation of radiation fog is known to be the cooling of air to its dewpoint, which is strongly dependent on temperature and relative humidity. In this section, a radiation fog event will be discussed in terms of urban expansion.

5.1. Description of case from 5 to 6 November 2016

From 5 to 6 November 2016, Shanghai was under the control of a weak high-pressure system, which is conducive for the formation of radiation fog. The wind speeds were below 2 m/s at XJH, SHA, and CM from 1500 on the 5th to 0900 on the 6th November 2016, where all times are China Standard Time (CST). The temperatures dropped rapidly by 7.4 °C at XJH, by 10.0 °C at SHA, and by 12.3 °C at CM. However, fog only occurred at CM, with the visibility decreasing below

Table 4
Numerical experiments and corresponding urban land use, AH, and atmospheric conditions (initial and boundary conditions of the atmosphere).

Case	Scenario	Urban land use	AH	Atmospheric conditions
URB1988	Past	1988	AH 1988 for LULC 1988	2013
LU2013	–	2013	AH 1988 for LULC 2013	2013
URB2013	Current	2013	AH 2013 for LULC 2013	2013

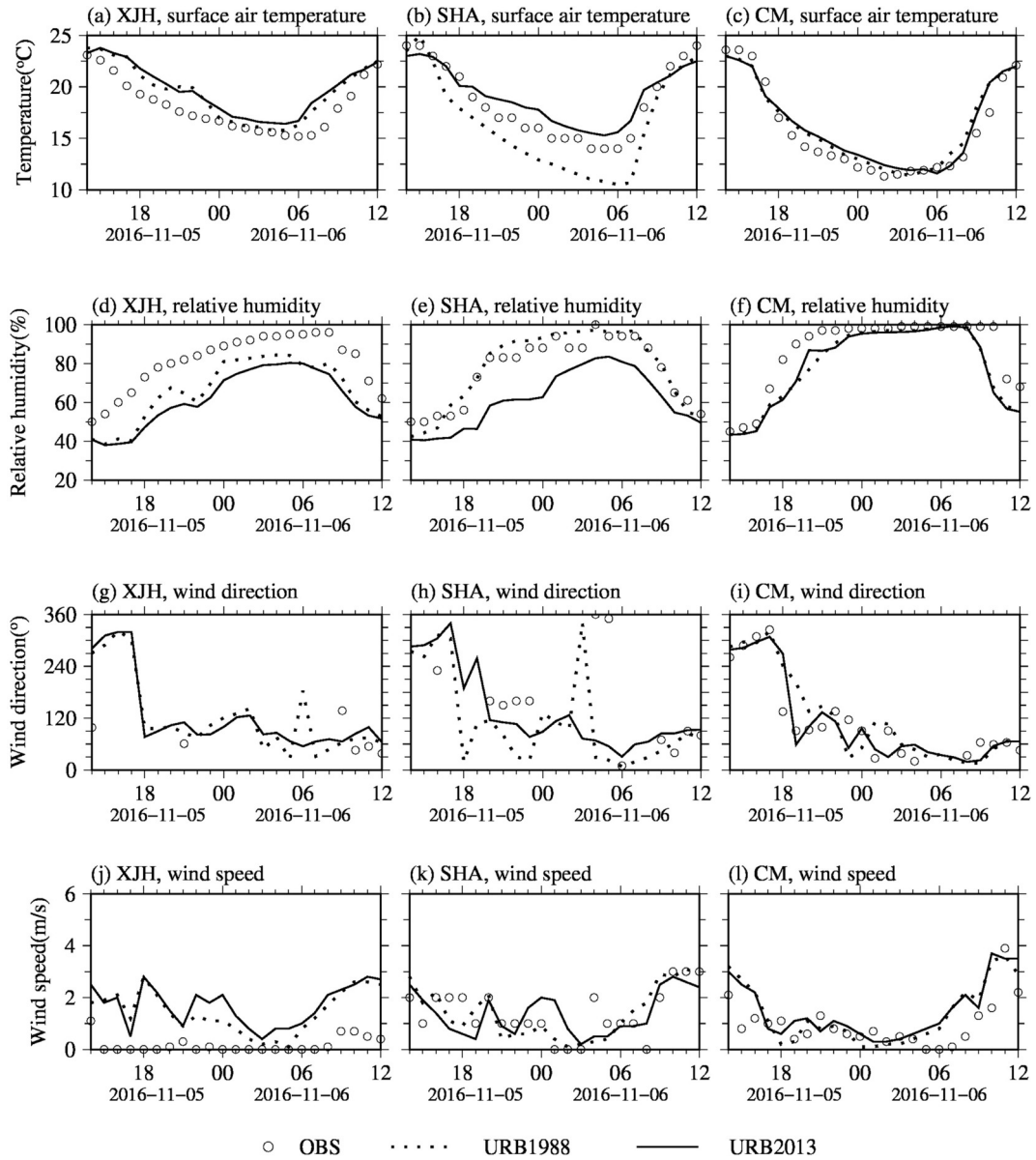


Fig. 8. Time series of the surface air temperature ($^{\circ}\text{C}$), relative humidity (%), wind direction ($^{\circ}$), and wind speed (m/s) at XJH, SHA, and CM stations during the radiation fog event. The circular symbols are observational data. The dotted and solid lines represent the simulated cases of URB1988 and URB2013.

1600 m at 2300 on the 5th, with a dense fog forming from 0100 to 0900 on the 6th.

5.2. Evaluation of the numerical simulation

To evaluate the model performance, we first compare the simulation results for case URB2013 to the hourly observations at the Shanghai stations. The results are averaged out over all eight ensemble members and shown in Fig. 8. To help evaluate the model performance, we list the correlation coefficients (R), biases (BIAS), and root mean square errors (RMSEs) of the model in Table 7.

Overall, the model reproduced well the general diurnal changes of the observed surface air temperature and relative humidity. The surface air temperatures are slightly overestimated with biases between 0.54 and 1.63°C , with RMSEs between 1.15 and 1.84°C , and a correlation coefficient over 0.94 at a significance level of 0.01 (Table 7). For relative humidity, the model made underestimates at all stations with mean biases between 7.7 and 19.3%, with RMSEs between 11.2 and 20.0%, and correlation coefficients of relative humidity over 0.91 at a

Table 7

Correlation coefficients (R), biases (BIAS), and root mean square errors (RMSEs) of the observed and simulated surface air temperatures ($^{\circ}\text{C}$) and relative humidity (%) for the radiation-fog case.

Station name	Surface air temperature			Relative humidity		
	R	BIAS ($^{\circ}\text{C}$)	RMSE ($^{\circ}\text{C}$)	R	BIAS (%)	RMSE (%)
XJH	0.94	1.63	1.84	0.94	-19.3	20.0
SHA	0.98	0.65	1.30	0.92	-15.1	16.5
CM	0.97	0.54	1.15	0.91	-7.7	11.2

significance level of 0.01 (Table 7). For wind speed and wind direction, during the first 5 h, the simulated wind speeds at XJH are higher and wind directions differ from observations. Thereafter, agreement improves. In contrast, the simulated wind directions and wind speeds at SHA and CM agree well with observations. Although we mention the comparison to observations, our discussion will focus on the urban impact (difference between cases URB1988 and URB2013).

Table 8
Visibility algorithms.

Abbreviation	Description of algorithm (unit: m)	Reference
UPP	$VIS_{\text{upp}} = 10^3 \times \min(24.135, -\ln(0.02)/\beta)$, $\beta = \beta_{\text{cw}} + \beta_{\text{rw}} + \beta_{\text{ci}} + \beta_{\text{sn}}$, $\beta_{\text{cw}} = 144.7C_{\text{cw}}^{0.88}$, $\beta_{\text{rw}} = 2.24C_{\text{cw}}^{0.75}$, $\beta_{\text{ci}} = 327.8C_{\text{ci}}^{1.00}$, $\beta_{\text{sn}} = 10.36C_{\text{sn}}^{0.7776}$.	NCEP Unified Post Processor versions 2.2 (UPP2.2)
RUC	$VIS_{\text{ruc}} = 10^3 \times 60 \times \exp[-2.5 \times (\text{RH} - 15) / 80]$, where RH is relative humidity (%).	Rapid Update Cycle (RUC) method
FSL	$VIS_{\text{fsl}} = 1609 \times 6000 \times (T - T_d) / RH^{1.75}$, where RH is relative humidity (%); T is surface air temperature ($^{\circ}\text{C}$); and T_d is dewpoint ($^{\circ}\text{C}$).	Doran et al. (1999)

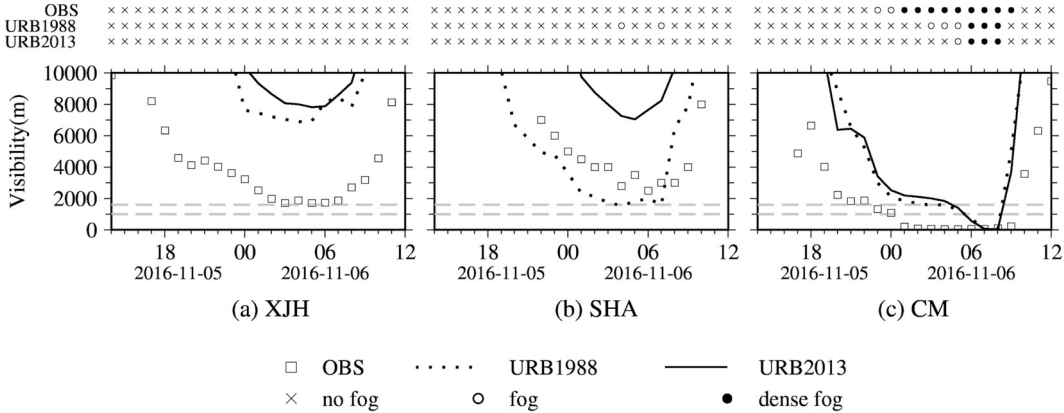


Fig. 9. Time series of the visibility (m) and fog occurrence at XJH, SHA, and CM stations during the radiation fog event. The circular symbols are observational data. The dotted and solid lines represent the simulated cases of URB1988 and URB2013.

The modelled fog occurrence is based on surface visibility. For each experiment, three surface visibilities were calculated based on the algorithms in Table 8, and then the minimum of the three was used to calculate the mean surface visibility of eight ensemble members for each case. Considering the significance of fog, we should not miss any fog events. If the mean value is used, the minimum value will be smoothed. We consider it more meaningful to use the minimum value instead of the average one. The results in Fig. 9 show no fog events in the simulations at XJH and SHA, in agreement with observations. At CM, both model and observations show fog, but the model underestimates the occurrence and duration of the fog.

Moreover, the spatial distributions of the observed and simulated surface air temperature, relative humidity, and visibility are shown in Figs. A.1 and A.2.

5.3. Impact of urban expansion on radiation fog

The simulations show that urban expansion should cause a slight increase in the surface visibility at XJH between 1988 and 2013 (Fig. 9a). For SHA, the simulations indicate that rapid urbanization greatly increases surface visibility for case URB2013, but even for case URB1988, no fog event is predicted in agreement with observations. As CM is the least urbanized among the three stations, the predicted period of fog is almost identical in both URB1988 and URB2013 (Fig. 9c). Overall, the urbanization has more influence on the rural–urban area (SHA) than on both the urbanized and rural areas (XJH and CM). Hereafter we discuss the thermodynamic effects of urban expansion on the decreased fog.

The most significant factor from urbanization on fog is the UHI effect, specifically, the increase in surface air temperature. Between URB1988 and URB2013, Fig. 8a,c show that the surface air temperatures at XJH and CM remain almost the same (0.3 °C for XJH and 0.04 °C for CM), but urbanization significantly increases the temperature at SHA (2.8 °C). In general, surface air temperature changes are largest for the area just surrounding the urban area in 1988 (Fig. 10a).

In particular, Fig. 10a shows that the simulated surface air temperatures increase in 2013 by 0.5 to 6.1 °C. As the simulated time is 2000 CST, the temperature increase indicates that nocturnal cooling has weakened due to urbanization, resulting from a warmer urban surface at SHA in 2013. For the formation of radiation fog, nocturnal cooling is critical, making the moist air near the ground cool to its dewpoint. So, when nocturnal cooling becomes weaker, the area is less conducive for fog formation.

A higher surface air temperature means a higher saturation vapor pressure of water. However, Fig. 10b shows that the surface water vapor density has decreased, in most areas by 0.5 g/kg or more (Fig. 10b), indicating a decrease in the vapor pressure of water. The temperature increase and vapor-pressure decrease both reduce the relative humidity, especially in rural–urban areas (Fig. 10c).

Another important condition for fog formation is the existence of an inversion or isothermal layer. The inversion or isothermal layer can trap moisture in the near-surface, which tends to cause the water vapor to accumulate. Fig. 11 shows the height–time cross-sections of the simulated temperature in cases of URB1988 and URB2013 at SHA during the radiation-fog event. Case URB1988 shows an inversion layer below 100 m, with an isothermal layer just above. However, due to the urbanization, case URB2013 shows a warmer near-surface layer. This warming weakens the inversion layer, essentially causing the inversion to vanish, making it more difficult for fog to form.

6. Advection fog case

Advection fog was the second most common fog in Shanghai from 2008 to 2017 (Fig. 3). The primary process of advection fog usually involves the vertical mixing of moist air parcels of different temperatures. In general, global warming should increase both sea and land surface temperatures and decrease their difference in temperature, an effect that should decrease the occurrence of advection fog. But how should urban expansion affect this fog? To address this question, we analyse the simulation of an observed advection fog.

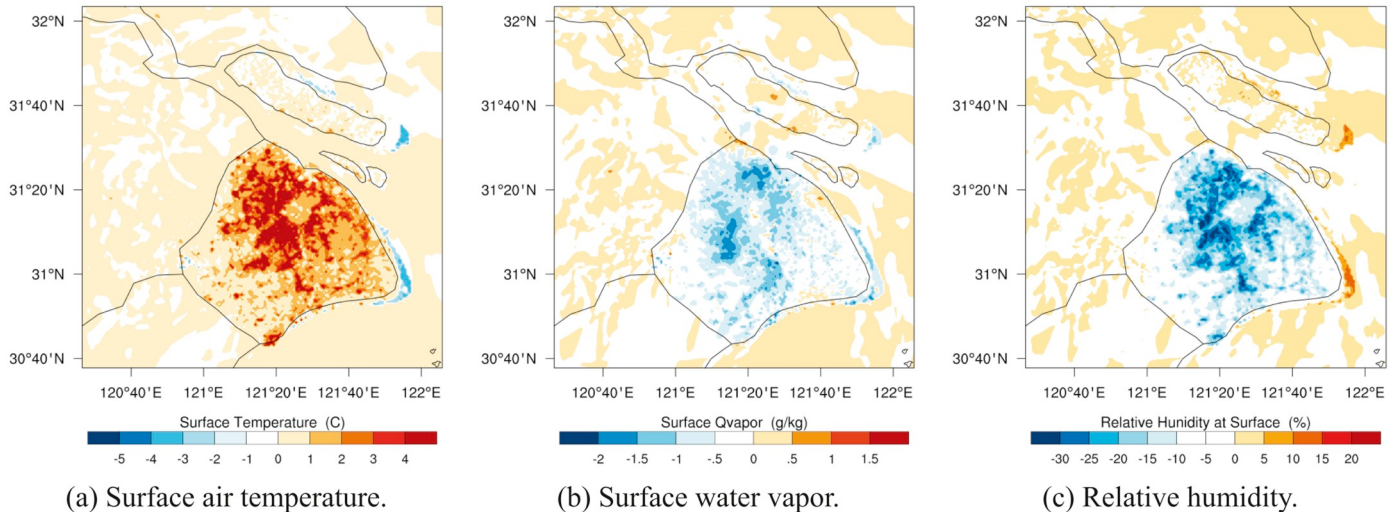


Fig. 10. Simulated differences between URB2013 and URB1988 cases. (a) Surface air temperature (°C). (b) Surface water vapor (g/kg). (c) Relative humidity (%). The time and date are 2000 CST 5 November 2016.

6.1. Description of case from 11 to 12 February 2016

On 11 February 2016, there was a high-pressure system east of Shanghai. Meanwhile, a depression developed in southwest China with an inverted trough extending north-easterly. Fog and precipitation occurred under the impact of the surface trough. Light rain was observed at SHA from 10 to 12 am on the morning of 11 February. A southeast wind was measured for the whole day, which facilitated the movement of warm, moist air masses from the East China Sea. At the CM station, visibility began to drop at 1900 CST on 11 February and rose after 1000 CST on 12 February (Fig. 13). At XJH and SHA stations, visibility declined after midnight and increased after 0600 CST on 12 February. Thus, the fog occurred earlier and lasted longer at CM than at XJH and SHA.

6.2. Evaluation of the numerical simulation

For this fog event, consider the observed and simulated meteorological variables at the three stations. The surface air temperature is underestimated by about 0.51 °C at XJH and about 0.17 °C at SHA, but overestimated by about 0.67 °C at CM (Fig. 12a–c). For temperature, the

correlation coefficients are between 0.84 and 0.91 °C at a significance level of 0.01, and RMSE ranges from 1.21 to 1.73 °C (Table 9). For the relative humidity, the model underestimated the relative humidity at all three stations (Fig. 12d–f), but the biases have a maximum of just 4.2%. The correlation coefficients are between 0.62 and 0.7 at a significance level of 0.01 and the RMSEs are between 8.0 and 9.0%. For wind, the observed wind directions fluctuate the most at XJH and CM, but the simulation show little variation at all three stations (Fig. 12g–i). In agreement with observations, the simulated wind directions are south-easterly, which facilitates advection from the sea. For wind speed, the simulations overestimate at XJH and CM, but underestimate at SHA (Fig. 12j–l).

Consider now the observed and simulated surface visibilities for the advection-fog event. The model underestimates the visibilities at XJH and SHA, but slightly overestimates visibility at CM (Fig. 13). Due to the underestimates, the modelled fog period is too long and with an onset that is too early at XJH and SHA. On the other hand, at the CM station, the simulated visibility agrees well with the observations, except it misses an abrupt break in the fog in the middle of the event. But overall, results show a well-modelled fog period and onset at CM.

Moreover, the spatial distributions of the observed and simulated

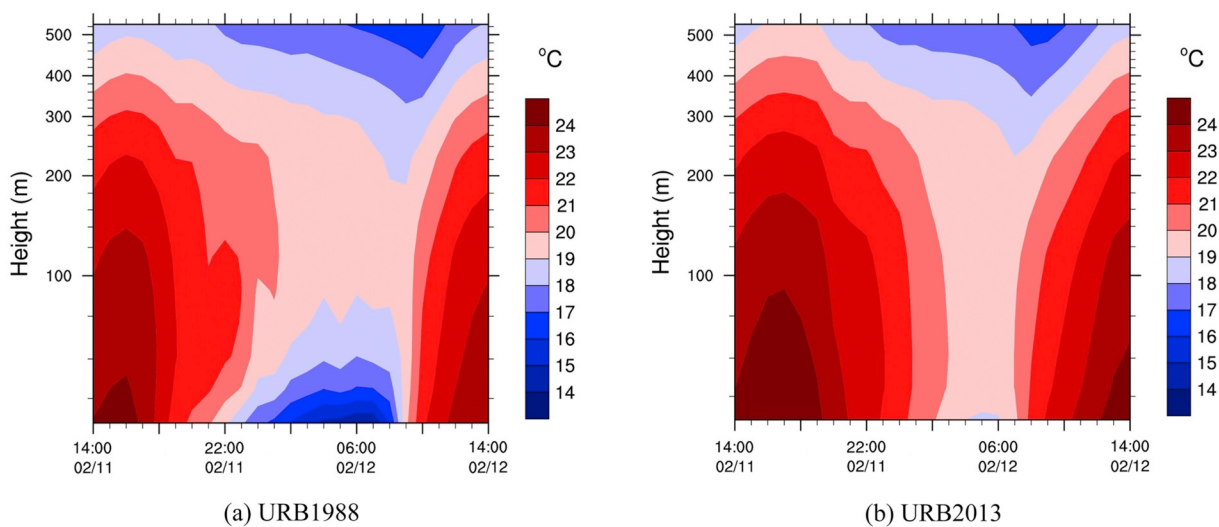


Fig. 11. Height-time cross-sections of the simulated temperature (°C) in URB1988 and URB2013 at SHA during the radiation-fog event (CST).

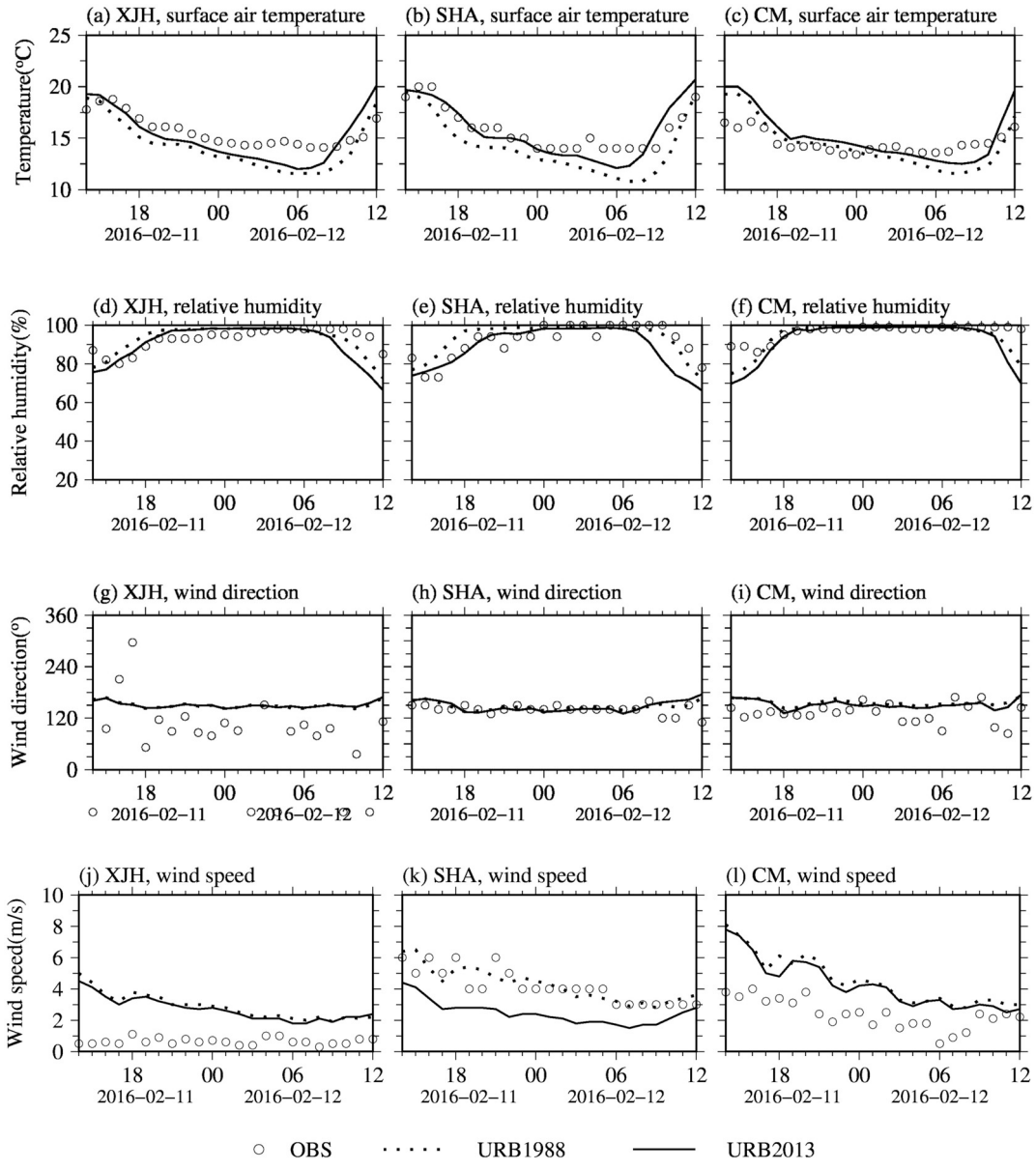


Fig. 12. Same as Fig. 8, but for the case of advection fog.

Table 9
Same as Table 7, but for a case of advection fog.

Station name	Surface air temperature			Relative humidity		
	R	BIAS (°C)	RMSE (°C)	R	BIAS (%)	RMSE (%)
XJH	0.84	-0.51	1.53	0.62	-2.3	8.0
SHA	0.91	-0.17	1.21	0.72	-3.3	8.1
CM	0.88	0.67	1.73	0.68	-4.2	9.0

surface air temperature, relative humidity, and visibility are shown in Figs. A.3 and A.4.

6.3. Impact of urban expansion on advection fog

The difference in simulations between the two years shows that urbanization increases the surface visibilities at XJH, SHA, and CM (Fig. 13). The largest increase occurs at SHA (rural–urban station), followed by XJH (urban), and CM (rural). The increased visibility shortens the fog periods, delays the onset of fog, and at XJH and SHA,

causes an early dissipation. For XJH, the onset is 1 h later (4 h for dense fog) and the dissipation 2 h earlier (Fig. 13a). For SHA, the onset is 6 h later (5 h for dense fog) and the dissipation 2 h earlier (Fig. 13b). On the other hand, for CM, the improved visibility has little effect on the onset and dissipation time (Fig. 13c). Overall, the urbanization greatly affects the rural–urban area, but only slightly affects the urbanized and rural areas.

To better understand these changes in visibility, we examine the liquid-water mixing ratio (LWMR), which must be non-zero when fog occurs. Thus, we examine the LWMR height–time cross-sections in Fig. 14. Fig. 14 shows the height–time cross-sections of the simulated LWMRs for the advection fog event. In case URB1988, the LWMR begins to accumulate at around 1800 CST, 11th Feb. and decreases rapidly at about 1000 CST, 12th Feb. The maxima (LWMR > 0.6 g/kg) appear at the height between 100 and 220 m at XJH and between 50 and 220 m at SHA and CM. However, in case URB2013, the LWMR accumulates later and less LWMR reaches the near-surface region than that in case URB1988. The liquid water tends to accumulate higher above the ground. The height of the maxima is between 150 and 220 m at XJH and between 130 and 220 m at CM. The intensities of the maxima

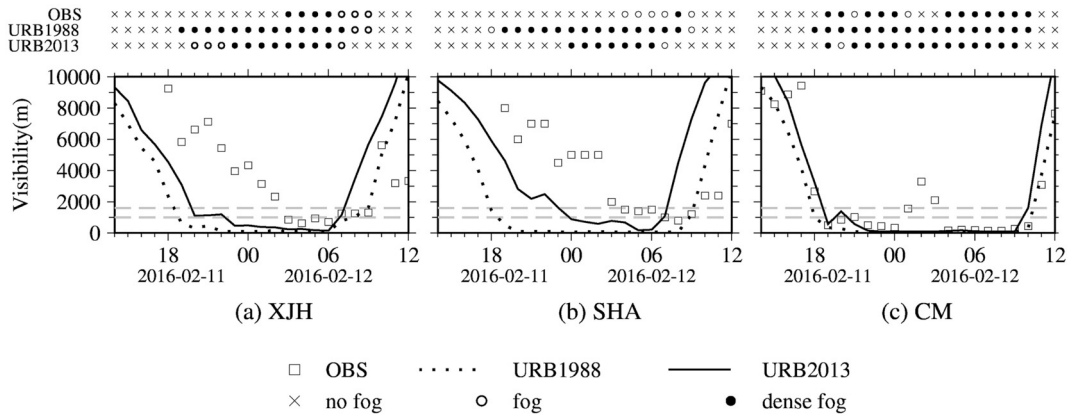


Fig. 13. Same as Fig. 9 but for the case of advection fog. Horizontal dashed lines show levels for fog occurrence and dense fog.

become weak at all three stations, maintaining $< 0.7 \text{ g/kg}$ and nearly vanish at SHA. Thus, the greatest change in LWMR appears in the rural–urban area.

However, the water-vapor mixing ratio has the opposite change, increasing at all three stations between the 1988 and 2013 simulations. Moreover, unlike the LWMR, the water-vapor mixing ratio is nearly uniform to about 150 m. At XJH and CM, the maximum water-vapor mixing ratios (12 g/kg for XJH, 10.5 g/kg for CM) last from 1500 to 1700 CST 11th Feb. in URB1988, but last longer in case URB2013, ending at 1800 CST 11th Feb. The slight change in the duration of the maximum water-vapor mixing ratio leads to a short delay of fog onset at

these two stations. At SHA, the water-vapor mixing ratio remains over 12 g/kg for 2 more hours in case URB2013 than in case URB1988. Moreover, the mixing ratio remains between 11.5 and 12 g/kg until 2000 CST 11th in URB1988, but until 2300 CST 11th in case URB2013. These changes lead to a 6-h delay of fog onset and a 5-h delay of dense fog occurrence (Fig. 13b). During the fog event, the minimum water vapor mixing ratio increases with urbanization for XJH and SHA. In particular, at XJH, the increase is about 0.5 g/kg, whereas at SHA, the increase is about 1 g/kg. However, the increase in water vapor is insufficient for the development of fog and results in the early dissipation of fog.

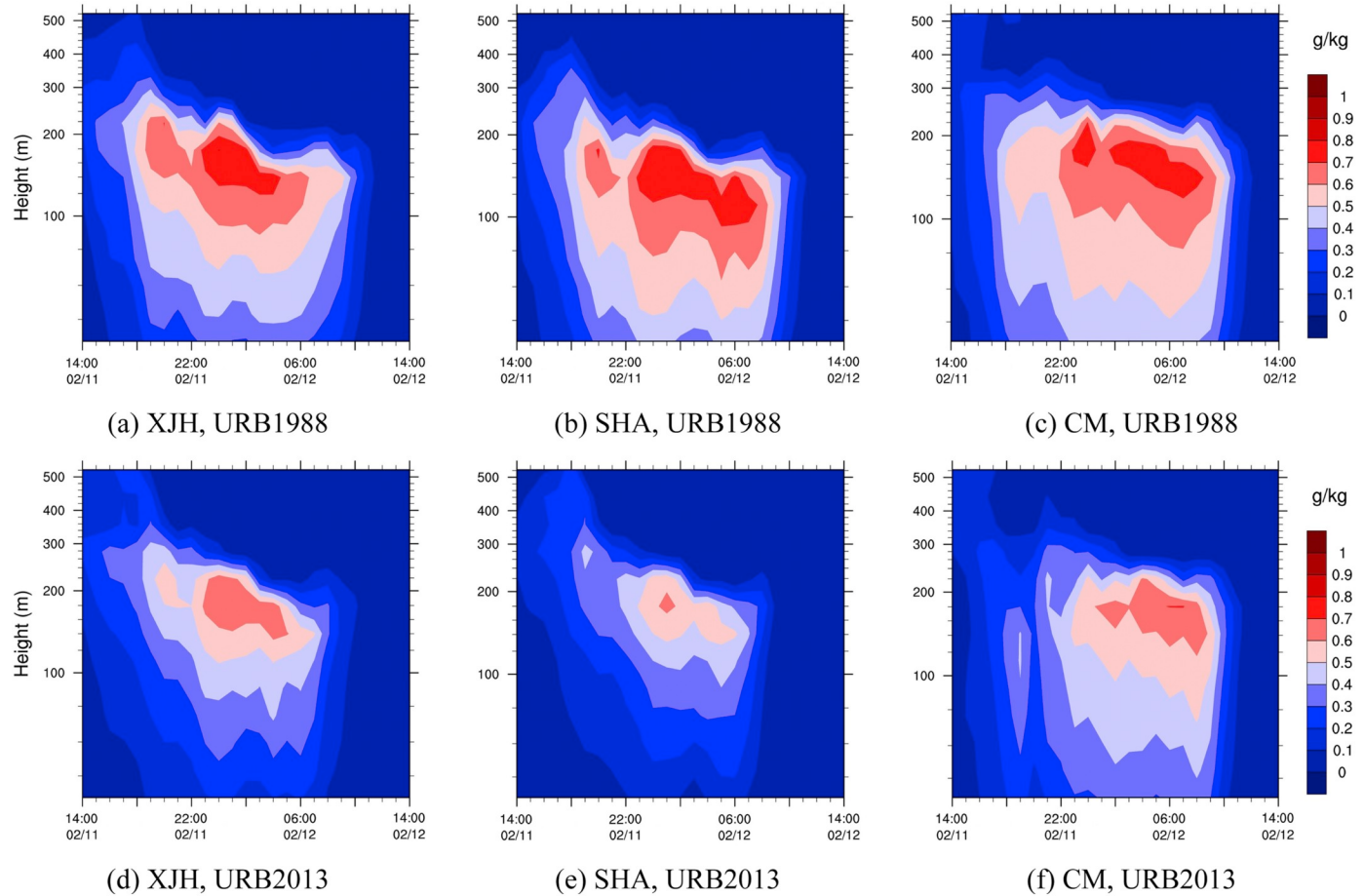


Fig. 14. Height–time cross-sections of the simulated liquid-water mixing ratios (g/kg) in URB1988 and URB2013 at XJH, SHA, and CM during the advection fog event.

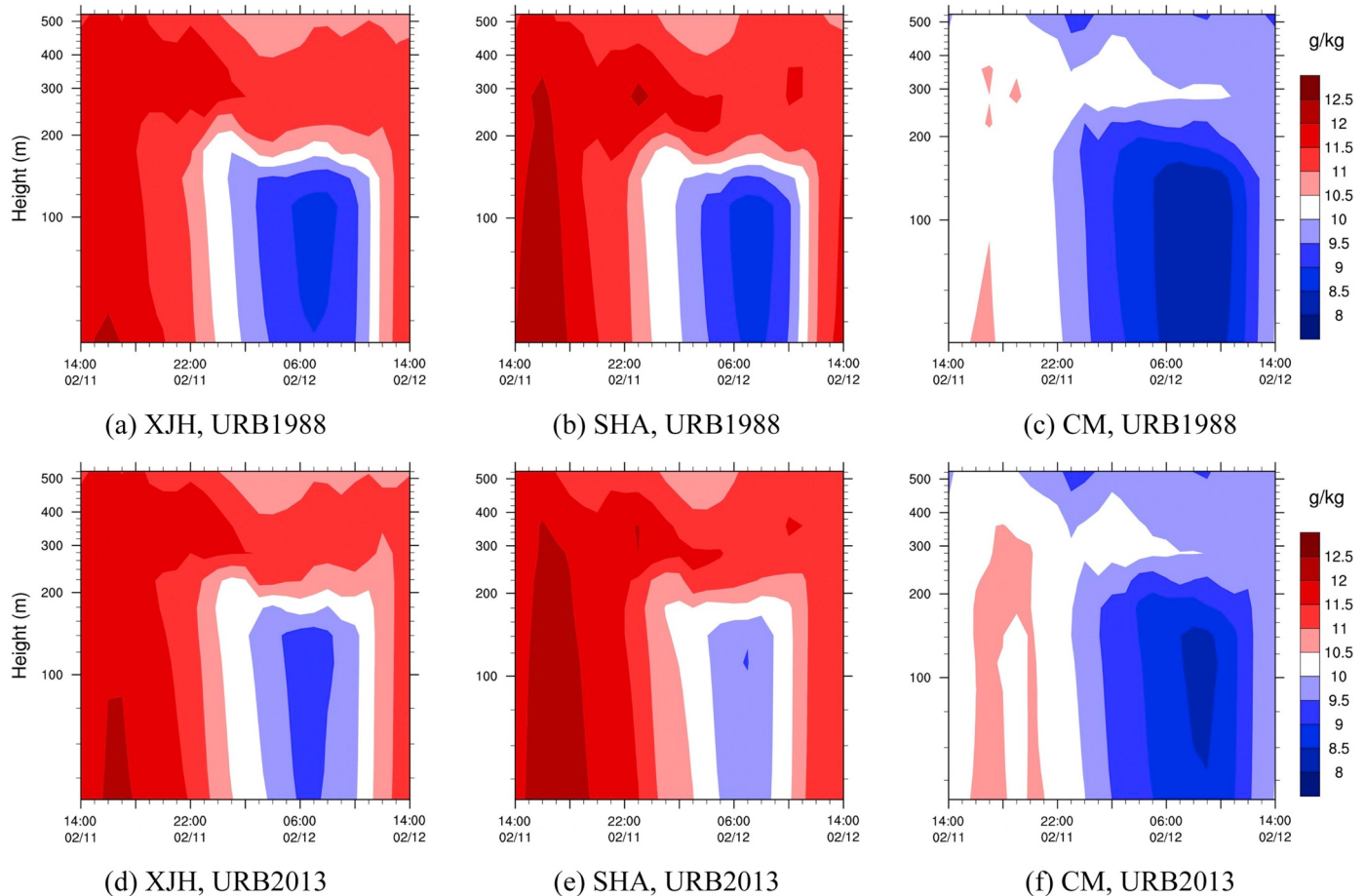


Fig. 15. Height-time cross-sections of the simulated water-vapor mixing ratios (g/kg) in URB1988 and URB2013 at XJH, SHA, and CM during the advection fog event.

Figs. 14 and 15 show that the urbanization would result in less water vapor condensing even though more water vapor is present. This behaviour may be explained by the increase in the mean surface air temperature by 0.9, 1.6, and 0.8 °C at XJH, SHA, and CM respectively (Fig. 12a–c). This role of temperature indicates that the surface air temperature is the dominant factor in the formation of advection fog.

Moreover, due to the higher surface air temperature, the near-surface air is heated by conduction as shown in Fig. 16. As a result, the urbanization delays the formation of the inversion layer by about 5 h and causes the inversion to vanish about 2 h earlier in case URB2013 than in case URB1988. Thus, the inversion layer exists for a shorter period.

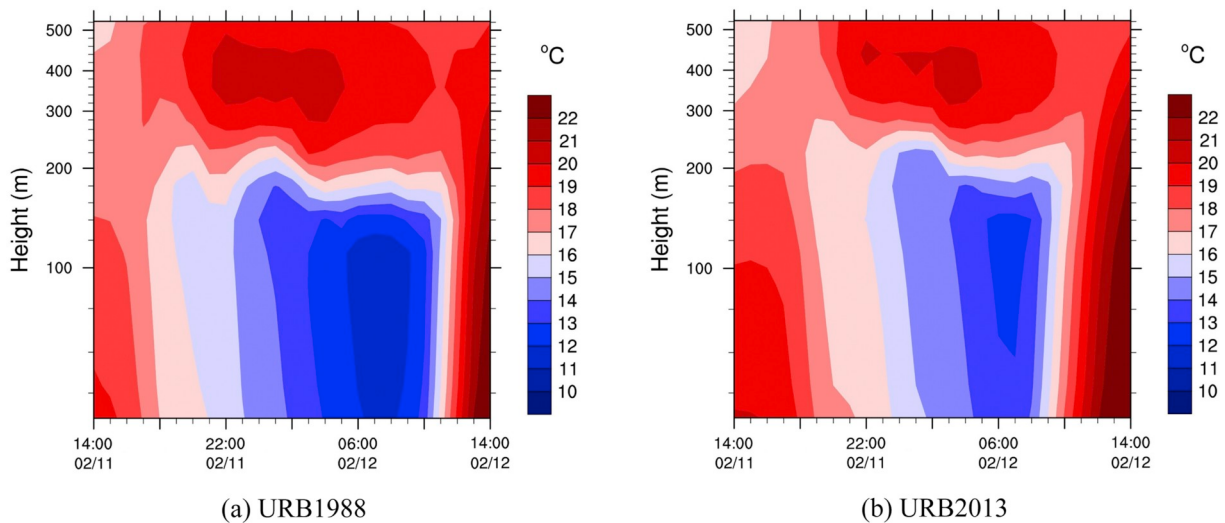


Fig. 16. Same as Fig. 11, but for the case of advection fog.

Table 10

Contributions of land-use change and AH-emission change to surface air temperature (°C).

Land-use	Radiation fog		Advection fog			
	AH	Total	Land-use	AH	Total	
Type I	-0.9	0.9	0	0.2	0.6	0.8
Type II	1.7	0.9	2.6	0.5	0.6	1.1
Type III	0.6	0.3	0.9	0.4	0.2	0.6
XJH	-1.2	1.5	0.3	0.4	0.5	0.9
SHA	1.4	1.4	2.8	0.9	0.7	1.6
CM	-0.2	0.3	0.1	0.7	0.2	0.9

7. Discussion

Of the two most common types of fog here, radiation and advection, both decreased due to a decrease in relative humidity and a diminished inversion layer. The weaker nocturnal cooling at the surface and a lower efficiency of the condensation from water vapor to liquid water are the other important influences on the changes in radiation fog and advection fog respectively. The main reason for these changes is the increase in surface air temperature.

In this study, sensitivity experiments were also conducted to examine the individual contributions of land-use and AH-emission change to the higher surface air temperature (Tables 4 and 5). Considering the systematic errors, we investigated mean surface air temperatures for three types of land-use change as well as for three representative stations. For the radiation fog event, the AH-emission change seems to make greater contribution than the land-use change for type I (Table 10). The negative temperatures might be caused by the decreased rate of AH emission as a result of the reduced urban fraction in the sensitivity experiments. However, land-use change tends to play more important role for type II and III. For the advection fog event, the contribution of AH-emission change is also greater than that of land-use change for type I. However, the result indicates the contrary for type III. The contribution of AH-emission change is comparable to that of land-use change for type II.

Studies of other locations link the decrease in the number of radiation fog events to the UHI effect (Sachweh and Koepke, 1995). In the UHI effect, changes in land use produce changes in the underlying heat capacity, latent-heat flux, and surface albedo. In addition, UHI includes an increase in AH that increases the surface heat flux, making the surface air warmer. From a thermodynamic viewpoint, our results show the relations between UHI and fog formation. More importantly, this study also presents the influence of UHI on advection fog. Urbanization decreases water vapor during the radiation fog case, but increases moisture in the advection fog case. For radiation fog, water vapor is related to latent heat. Urbanization increases surface air temperature, weakening the nocturnal cooling. The decreased cooling causes less condensation. As a result, less latent heat is released, indicating the decrease in water vapor. For advection fog, the saturation vapor pressure of water is related to temperature. The higher the temperature is, the higher the saturation vapor pressure of water will be. The air tends to contain more water vapor and becomes unsaturated, leading to less condensation. For advection fog, water vapor is transported from sea. The amount of water vapor is determined by its state change instead of latent heat.

The issues associated with urban expansion are not confined to land use and AH. The urbanization also induces an increase in aerosols, which play a significant role in the formation of fog (Twomey, 2007;

IPCC, 2007; Vautard et al., 2009; Van Oldenborgh et al., 2010; Niu et al., 2010; Baldocchi and Waller, 2014; Gao et al., 2015; Klemm and Lin, 2016; Lee et al., 2016; Zhong et al., 2018). The 2007 IPCC report (IPCC, 2007) indicated that aerosols could have either positive or negative net forcing in the range from -0.7 to +0.1 W·m⁻². Gao et al. (2015) used WRF-Chem to present a significant negative radiative forcing of aerosols by -20 to -140 W·m⁻² at the surface and a large positive radiative forcing by 20–120 W·m⁻², corresponding to a decrease in temperature by 0.8–2.8 °C at the surface, an increase in temperature by 0.1–0.5 °C at around 925 hPa, an increase in RH by about 4–12% at the surface and a decrease in RH by 1–6% at around 925 hPa. Klemm and Lin (2016) pointed out that 0.1 °C increase in temperature has about the same effect as 10% reduction of aerosols concentrations on fog decrease. It is clear that not only land use and AH but also aerosols are changing the meteorological variables. Meanwhile, the effects of aerosols on fog remain an open problem.

Many fog events described here formed in a region with a high concentration of PM2.5 and other air pollutants under certain meteorological conditions. Previous studies have also found that the regions in Shanghai with greater air pollution are where the fog occurs (Zhang et al., 2014b; Leng et al., 2014; Shen et al., 2015; Hu et al., 2016). However, the algorithms for calculating the surface visibility here did not include the direct effect from these aerosols, leading to a likely overestimate of the surface visibility. However, it is very difficult to solve the all issues by one study, thus most of the studies focus on one or a few selected issues. It is important to point out such study limitations and other important issues in the article, and how those may be addressed or solved in future studies.

Moreover, in this study, AH is added to the surface-layer atmosphere as the sensible heat flux. According to Moriwaki et al. (2008), AH is partitioned to 99.5%, 90%, and 65% of the sensible heat flux in Tokyo in winter, spring, and summer, respectively. Consequently, impacts of AH on the urban temperature (humidity) is slightly overestimated (underestimated) in the experiments and the urbanization effects on fog is overestimated in the simulations and experiments.

8. Conclusions

We examined 29 years of observations (1989–2017) of fog events in Shanghai, China, revealing a decreasing trend of four types of fog. Moreover, we used the WRF-UCM model with data on land use and anthropomorphic heat (AH) to examine in detail how urbanization affected the different types of fog. In particular, sensitivity experiments for a radiation fog and an advection fog were done for two urban scenario cases representing 1988 and 2013. Our key results are summarized as follows:

- (1) Among current fog events, the most common fog is radiation fog at 38.3% of the events, followed by advection fog at 27.7%, and advection–radiation fog at 23.4%. The least common type is precipitation fog at 8.5%.
- (2) Fog events have decreased in the past 29 years. For example, 248 events were identified in 1989–1998. However, only 47 events were identified in 2008–2017. The reduction in winter accounts for 50.2% of the total reduction, followed by spring with 26.9%.
- (3) Of all fog types, radiation-fog events decreased the most. Its decline is responsible for the decline of fog events in winter. Nevertheless, radiation fog remains the most common type.
- (4) The WRF-UCM model can reproduce radiation fog and advection fog.
- (5) The present study showed that the urban expansion tends to induce

an increase in surface air temperature by 0.5 to 6.1 °C at night, reducing the nocturnal cooling at the surface and water vapor density by 0.5 g/kg or more. The higher surface air temperature and lower water-vapor mixing ratio can suppress the formation of radiation fog.

- (6) The present study also revealed that the urban expansion seems to increase the mean surface air temperature by 0.8 to 1.6 °C for the advection fog event, allowing a rise in water-vapor mixing ratio by at least 0.5 g/kg. The higher surface air temperature and water-vapor mixing ratio could indicate less condensation into liquid water. It is also responsible for the decrease in relative humidity.
- (7) In both cases, the higher surface air temperature can warm the near-surface air, weakening the inversion layer.

Appendix A. Appendix

Figures of spatial distribution

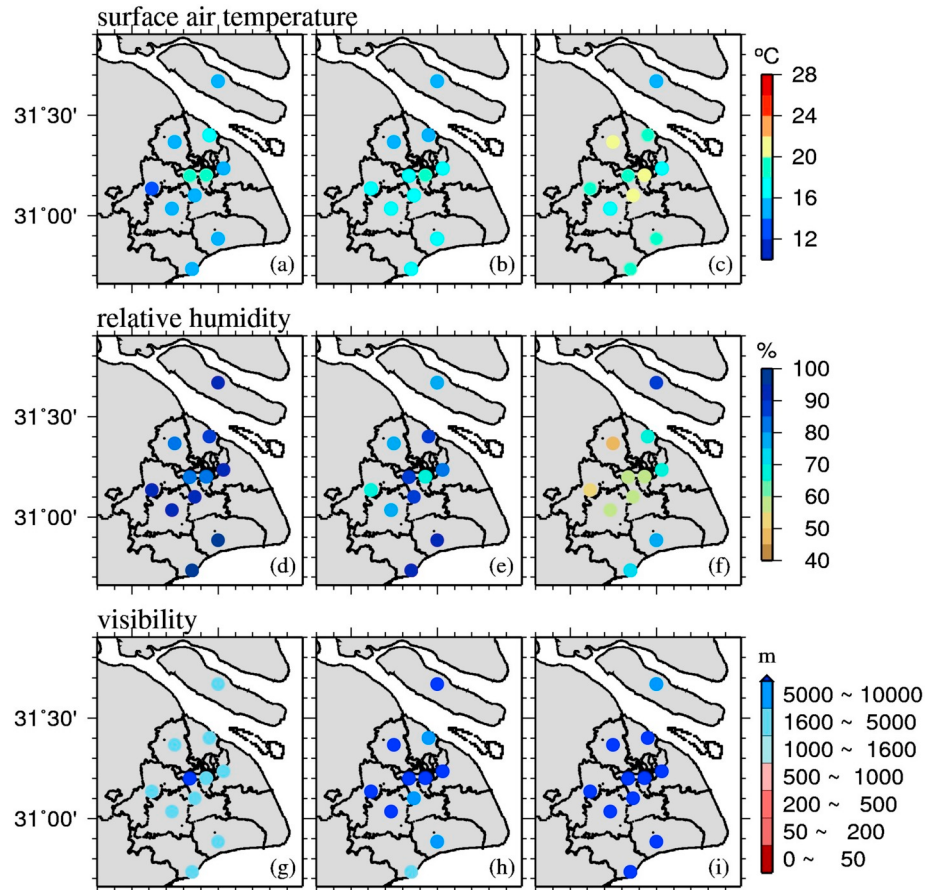


Fig. A.1. Spatial distribution of the observed and simulated surface air temperature (°C), relative humidity (%), and visibility (m) during the radiation fog event. The time and date are 2000 CST 5 November 2016.

The conclusions are based on these case studies only and future studies are needed to facilitate general conclusions.

Acknowledgments

The work was supported by the program called “Overseas visiting study program for young and middle-aged teachers in universities in Shanghai 2017”. We thank Hao Gong from University of Tsukuba for LULC data and instructions in GIS processing, Prof. Jiong Shu from East China Normal University for sharing the high-performance computer cluster, and Wenjuan Huang from Shanghai Climate Center, Shanghai Meteorological Services, Shanghai for data collection.

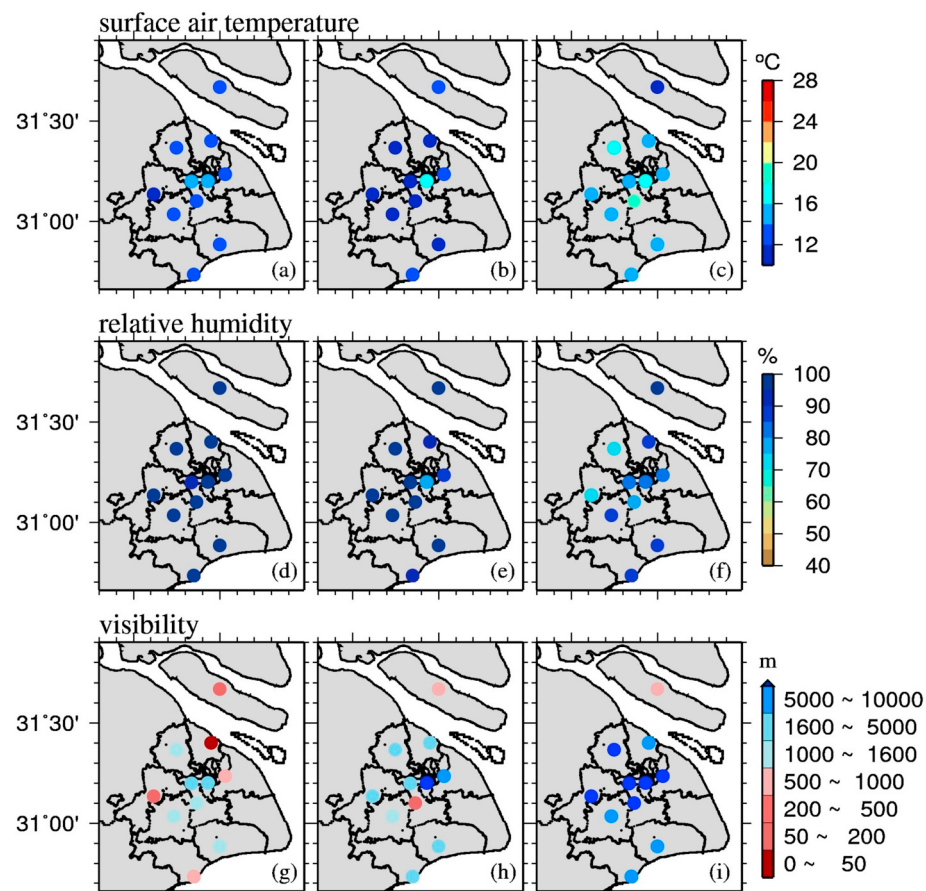


Fig. A.2. Same as Fig. A.1 but for 0600 CST 6 November 2016.

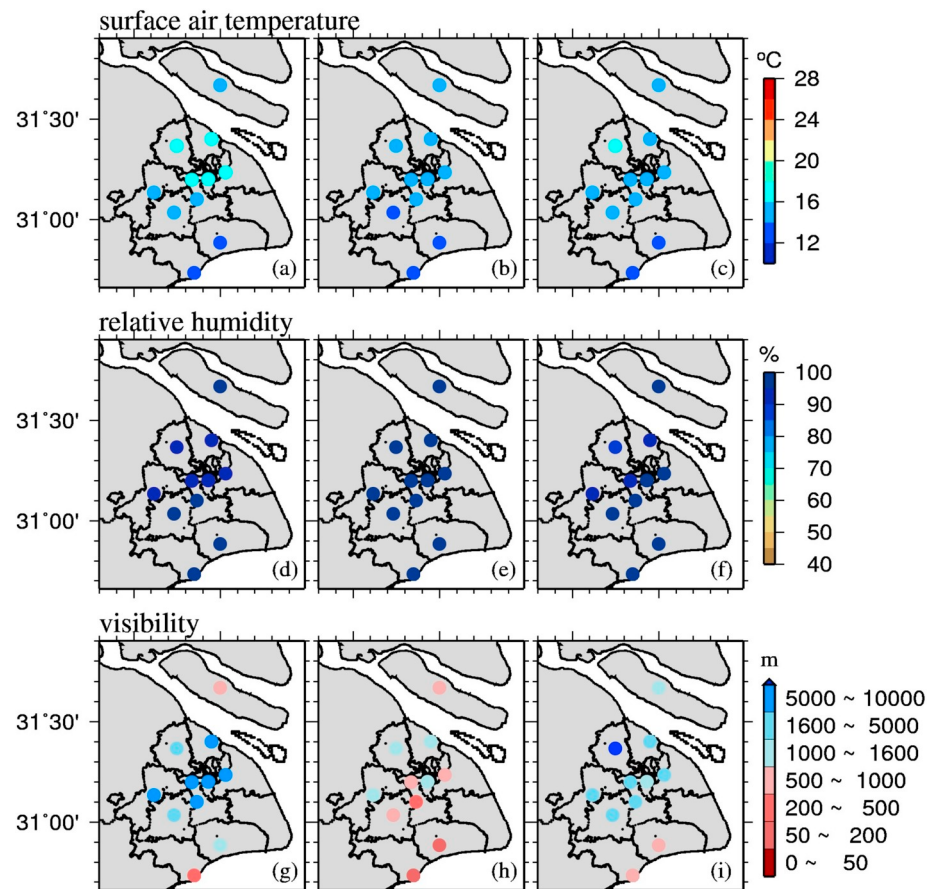


Fig. A.3. Same as Fig. A.1 but for the case of advection fog. The time and date are 2000 CST 11 February 2016.

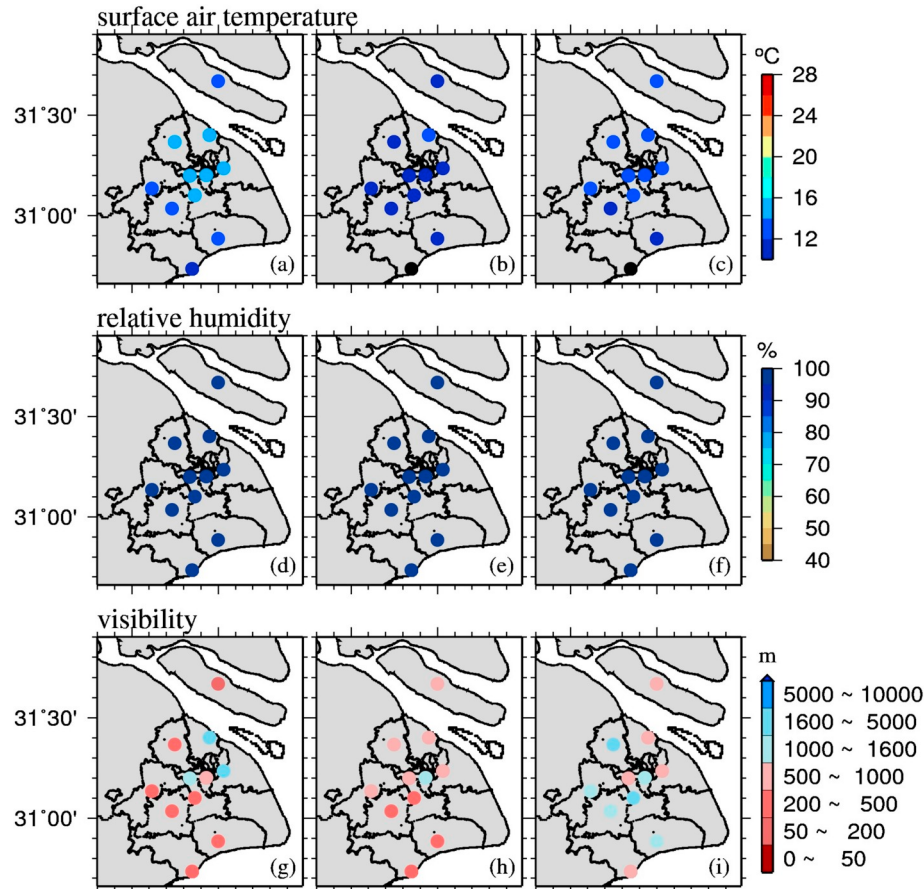


Fig. A.4. Same as Fig. A.3 but for 0600 CST 12 February 2016.

References

- Akimoto, Y., Kusaka, H., 2015. A climatological study of fog in Japan based on event data. *Atmos. Res.* 151, 200–212. <https://doi.org/10.1016/j.atmosres.2014.04.003>.
- Baldocchi, D., Waller, E., 2014. Winter fog is decreasing in the fruit growing region of the Central Valley of California. *Geophys. Res. Lett.* 41, 3251–3256. <https://doi.org/10.1002/2014GL060018>.
- Belorid, M., Lee, C.B., Kim, J.C., Cheon, T.H., 2015. Distribution and long-term trends in various fog types over South Korea. *Theor. Appl. Climatol.* 122, 699–710. <https://doi.org/10.1007/s00704-014-1321-x>.
- Byers, H.R., 1959. *General Meteorology*, 4th Edn. McGraw-Hill, New York, pp. 277–279.
- Chaochua, N., Temimi, M., Weston, M., Ghedira, H., 2017. Sensitivity of the meteorological model WRF-ARW to planetary boundary layer schemes during fog conditions in a coastal arid region. *Atmos. Res.* 187, 106–127. <https://doi.org/10.1016/j.atmosres.2016.12.009>.
- Chen, S., Shi, Y., Wang, L., Dong, A., 2006. Impact of climate variation on fog in China. *J. Geogr. Sci.* 16, 430–438.
- Doan, Q.-V., Kusaka, H., 2016. Numerical study on regional climate change due to the rapid urbanization of greater Ho Chi Minh City's metropolitan area over the past 20 years. *Int. J. Climatol.* 36, 3633–3650. <https://doi.org/10.1002/joc.4582>.
- Doran, J.A., Roehr, P.J., Bebervyk, D.J., Brooks, G.R., Gayno, G.A., Williams, R.T., Lewis, J.M., Lefevre, R.J., 1999. The MM5 at the Air Force Weather Agency-New products to support military operations. In: *The 8th Conference on Aviation, Range, and Aerospace Meteorology*. NOAA/NWS, Dallas, Texas.
- Dupont, J.C., Haefelin, M., Stolaki, S., Elias, T., 2016. Analysis of dynamical and thermal processes driving fog and quasi-fog life cycles using the 2010–2013 ParisFog dataset. *Pure Appl. Geophys.* 173, 1337–1358. <https://doi.org/10.1007/s00024-015-1159-x>.
- Forthun, G.M., Johnson, M.B., Schmitz, W.G., Blume, J., Caldwell, R.J., 2006. Trends in fog frequency and duration in the Southeast United States. *Phys. Geogr.* 27, 206–222. <https://doi.org/10.2747/0272-3646.27.3.206>.
- Fu, G.Q., Xu, W.Y., Yang, R.F., Li, J.B., Zhao, C.S., 2014. The distribution and trends of fog and haze in the North China Plain over the past 30 years. *Atmos. Chem. Phys.* 14, 11949–11958. <https://doi.org/10.5194/acp-14-11949-2014>.
- Gao, Y., Zhang, M., Liu, Z., Wang, L., Wang, P., Xia, X., Tao, M., Zhu, L., 2015. Modeling the feedback between aerosol and meteorological variables in the atmospheric boundary layer during a severe fog-haze event over the North China Plain. *Atmos. Chem. Phys.* 15, 4279–4295. <https://doi.org/10.5194/acp-15-4279-2015>.
- Gong, H., Simwanda, M., Murayama, Y., 2017. An Internet-based GIS Platform Providing Data for Visualization and Spatial Analysis of Urbanization in Major Asian and African Cities. *ISPRS Int. J. Geo-Information* 6, 257. <https://doi.org/10.3390/ijgi6080257>.
- Hu, Q., Fu, H., Wang, Z., Kong, L., Chen, M., Chen, J., 2016. The variation of characteristics of individual particles during the haze evolution in the urban Shanghai atmosphere. *Atmos. Res.* 181, 95–105. <https://doi.org/10.1016/j.atmosres.2016.06.016>.
- IPCC, 2007. *Climate change 2007—the physical science basis: Working group I contribution to the fourth assessment report of the IPCC*. Cambridge University Press, pp. 153–185.
- Jin, L., Shi, J., 2008. Climatic Characteristics and Change Laws of fog and Haze Days in Shanghai. *Plateau Meteor.* 27, 138–143 in Chinese.
- Klemm, O., Lin, N.H., 2016. What causes observed fog trends: Air quality or climate change? *Aerosol Air Qual. Res.* 16, 1131–1142. <https://doi.org/10.4209/aaqr.2015.05.0353>.
- Kusaka, H., Kondo, H., Kikegawa, Y., Kimura, F., 2001. A simple single-layer urban canopy model for atmospheric models: comparison with multi-layer and slab models. *Bound.-Layer Meteorol.* 101, 329–358. <https://doi.org/10.1023/A:1019207923078>.
- LaDochy, S., Witiw, M., 2012. The continued reduction in dense fog in the southern California region: possible causes. *Pure Appl. Geophys.* 169, 1157–1163. <https://doi.org/10.1007/s00024-011-0366-3>.
- Lee, H.H., Chen, S.H., Kleeman, M.J., Zhang, H., DeNero, S.P., Joe, D.K., 2016. Implementation of warm-cloud processes in a source-oriented WRF/Chem model to study the effect of aerosol mixing state on fog formation in the Central Valley of California. *Atmos. Chem. Phys.* 16, 8353–8374. <https://doi.org/10.5194/acp-16-8353-2016>.
- Leng, C., Zhang, Q., Zhang, D., Xu, C., Cheng, T., Zhang, R., Tao, J., Chen, J., Zha, S., Zhang, Y., Li, X., Kong, L., Gao, W., 2014. Variations of cloud condensation nuclei (CCN) and aerosol activity during fog-haze episode: a case study from Shanghai. *Atmos. Chem. Phys.* 14, 12499–12512. <https://doi.org/10.5194/acp-14-12499-2014>.
- Li, Z.H., Yang, J., Shi, C.E., Pu, M.J., 2012. Urbanization effects on fog in China: Field research and modeling. *Pure Appl. Geophys.* 169, 927–939. <https://doi.org/10.1007/s00024-011-0356-5>.
- Lin, C., Zhang, Z., Pu, Z., Wang, F., 2017. Numerical simulations of an advection fog event over Shanghai Pudong International Airport with the WRF model. *J. Meteorol. Res.* 31, 874–889. <https://doi.org/10.1007/s13351-017-6187-2>.
- Moriwaki, R., Kanda, M., Senoo, H., Hagishima, A., 2008. Anthropogenic water vapour

- emissions in Tokyo. *Water Resour. Res.* 44, W11424. <https://doi.org/10.1029/2007WR006624>.
- Niu, F., Li, Z., Li, C., Lee, K.H., Wang, M., 2010. Increase of wintertime fog in China: potential impacts of weakening of the Eastern Asian monsoon circulation and increasing aerosol loading. *J. Geophys. Res. Atmos.* 115, 1–12. <https://doi.org/10.1029/2009JD013484>.
- Sachweh, M., Koepke, P., 1995. Radiation fog and urban climate. *Geophys. Res. Lett.* 22, 1073–1076. <https://doi.org/10.1029/95GL00907>.
- Seidel, T.M., Grant, A.N., Pszenny, A.A.P., Allman, D.J., 2007. Dewpoint and humidity measurements and trends at the summit of Mount Washington, New Hampshire, 1935–2004. *J. Clim.* 20, 5629–5641. <https://doi.org/10.1175/2007JCLI1604.1>.
- Shen, X.J., Sun, J.Y., Zhang, X.Y., Zhang, Y.M., Zhang, L., Che, H.C., Ma, Q.L., Yu, X.M., Yue, Y., Zhang, Y.W., 2015. Characterization of submicron aerosols and effect on visibility during a severe haze-fog episode in Yangtze River Delta, China. *Atmos. Environ.* 120, 307–316. <https://doi.org/10.1016/j.atmosenv.2015.09.011>.
- Shi, C., Roth, M., Zhang, H., Li, Z., 2008. Impacts of urbanization on long-term fog variation in Anhui Province, China. *Atmos. Environ.* 42, 8484–8492. <https://doi.org/10.1016/j.atmosenv.2008.08.002>.
- Stolaki, S.N., Kazadzis, S.A., Foris, D.V., Karacostas, T.S., 2009. Fog characteristics at the airport of Thessaloniki, Greece. *Nat. Hazards Earth Syst. Sci.* 9, 1541–1549. <https://doi.org/10.5194/nhess-9-1541-2009>.
- Syed, F.S., Körnich, H., Tjernström, M., 2012. On the fog variability over South Asia. *Clim. Dyn.* 39, 2993–3005. <https://doi.org/10.1007/s00382-012-1414-0>.
- Tardif, R., Rasmussen, R.M., 2007. Event-based climatology and typology of fog in the New York City region. *J. Appl. Meteorol. Climatol.* 46, 1141–1168. <https://doi.org/10.1175/JAM2516.1>.
- Twomey, S., 2007. Pollution and the Planetary Albedo. *Atmos. Environ.* 41, 120–125.
- <https://doi.org/10.1016/j.atmosenv.2007.10.062>.
- Van Oldenborgh, G.J., Yiou, P., Vautard, R., 2010. On the roles of circulation and aerosols in the decline of mist and dense fog in Europe over the last 30 years. *Atmos. Chem. Phys.* 10, 4597–4609.
- Vautard, R., Yiou, P., Van Oldenborgh, G.J., 2009. Decline of fog, mist and haze in Europe over the past 30 years. *Nat. Geosci.* 2, 115–119. <https://doi.org/10.1038/ngeo414>.
- Williams, A.P., Schwartz, R.E., Iacobellis, S., Seager, R., Cook, B.I., Still, C.J., Husak, G., Michaelsen, J., 2015. Urbanization causes increased cloud base height and decreased fog in coastal Southern California. *Geophys. Res. Lett.* 42, 1527–1536. <https://doi.org/10.1002/2015GL063266>.
- Witiw, M.R., LaDochy, S., 2008. Trends in fog frequencies in the Los Angeles Basin. *Atmos. Res.* 87, 293–300. <https://doi.org/10.1016/j.atmosres.2007.11.010>.
- Zhang, R.H., Li, Q., Zhang, R.N., 2014a. Meteorological conditions for the persistent severe fog and haze event over eastern China in January 2013. *Sci. China Earth Sci.* 57, 26–35. <https://doi.org/10.1007/s11430-013-4774-3>.
- Zhang, X., Musson-Genon, L., Dupont, E., Milliez, M., Carissimo, B., 2014b. On the Influence of a simple Microphysics Parametrization on Radiation fog Modelling: a Case Study during ParisFog. *Boundary-Layer Meteorol.* 151, 293–315. <https://doi.org/10.1007/s10546-013-9894-y>.
- Zhong, J., Zhang, X., Wang, Y., Liu, C., Dong, Y., 2018. Heavy aerosol pollution episodes in winter Beijing enhanced by radiative cooling effects of aerosols. *Atmos. Res.* 209, 59–64. <https://doi.org/10.1016/j.atmosres.2018.03.011>.
- Zhou, S., Zheng, J., 1987. Shanghai urban influence of fog. *Acta Meteor. Sinica (in Chinese)* 45, 366–369. <https://doi.org/10.11676/qxb1987.047>.
- Zhou, S., Zhang, X., Guo, S., 1981. On the formation and classification of fogs of Shanghai. *In: Chinese. Trans. Oceanol. Limnology (1)*, 11–18. <https://doi.org/10.13984/j.cnki.cn37-1141.1981.01.002>.